Environmental Pollution 344 (2024) 123318

Contents lists available at ScienceDirect

Environmental Pollution

journal homepage: www.elsevier.com/locate/envpol

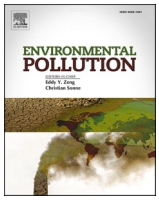

The change of coordination environments induced by vacancy defects in hematite leads to a contrasting difference between cation Pb(II) and oxyanion As(V) immobilization☆

Yongjin Xiang [a], Juan Liu [a], Yiwen Chen [b], Hongjun Zhang [b], Lu Ren [c], Bangjiao Ye [b], Wenfeng Tan [a], Kappler Andreas [d], Jingtao Hou [a,*]

[a] State Environmental Protection Key Laboratory of Soil Health and Green Remediation, Hubei Key Laboratory of Soil Environment and Pollution Remediation, College of Resources and Environment, Huazhong Agricultural University, Wuhan, 430070, China
[b] State Key Laboratory of Particle Detection and Electronics, University of Science and Technology of China, Hefei, 230026, China
[c] School of Civil Engineering, Suzhou University of Science and Technology, Suzhou, 215009, China
[d] Geomicrobiology, Department of Geosciences, University of Tuebingen, Tuebingen, 72076, Germany

ARTICLE INFO

Keywords:
Iron oxide
Vacancy defect
Arsenate
Lead
Mobility

ABSTRACT

Hematite is an iron oxide commonly found in terrestrial environments and plays an essential role in controlling the migration of heavy metal(loid)s in groundwater and sediments. Although defects were shown to exist both in naturally occurring and laboratory-synthesized hematite, their influences on the immobilization of heavy metal (loid)s remain poorly understood. In this study, hematite samples with tunable vacancy defect concentrations were synthesized to evaluate their adsorption capacities for the cation Pb(II) and for the oxyanion As(V). The defects in hematite were characterized using XRD, TEM-EDS mapping, position annihilation lifetime spectroscopy, and XAS. The surface charge characteristics in defective hematite were investigated using zeta potential measurements. We found that Fe vacancies were the primary defect type in the hematite structure. Batch experiments confirmed that Fe vacancies in hematite promoted As(V) adsorption, while they decreased Pb(II) adsorption. The reason for the opposite effects of Fe vacancies on Pb(II) and As(V) immobilization was investigated using DFT calculations and EXAFS analysis. The results revealed that Fe vacancies altered As–Fe coordination from a monodentate to a bidentate complex and increased the length of the Pb–Fe bond on the hematite surface, thereby leading to an increase in As(V) bonding strength, while decreasing Pb(II) adsorption affinity. In addition, the zeta potential analysis demonstrated that the presence of Fe vacancies led to an increase in the isoelectric point (IEP) of hematite samples, which therefore decreased the attraction for the cation Pb(II) and increased the attraction for the oxyanion As(V). The combination of these two effects caused by defects contributed to the contrasting difference between cation Pb(II) and oxyanion As(V) immobilization by defective hematite. Our study therefore provides new insights into the migration and fate of toxic heavy metal(loid)s controlled by iron minerals.

1. Introduction

Heavy metal and metalloid pollution in groundwater resulting from sewage irrigation, industrial emission, atmospheric deposition, and mining has received much attention due to the substantial threats to human health through the food chain(Harsha et al., 2019; Li et al., 2014). Naturally occurring iron (oxyhydr)oxide minerals such as hematite (α-Fe_2O_3) are widely distributed in natural environments and have been shown to affect the migration of heavy metal(loid)s because of their high reactivities (Cornell and Schwertmann, 2003), thereby controlling the risk and fate of heavy metal(loid)s, especially for the heavy metal cation lead (Pb(II)) (Liang et al., 2021; Qiu et al., 2020) and the metalloid oxyanion arsenic (As) (Guo et al., 2007; Iorio et al., 2018; Yan et al., 2020). However, Fe-bearing minerals with a perfect crystal structure are usually not observed in natural environments due to fluctuations in redox conditions, weathering, and the incorporation of

☆ This paper has been recommended for acceptance by Hefa Cheng.

* Corresponding author.
E-mail address: houjt87@163.com (J. Hou).

https://doi.org/10.1016/j.envpol.2024.123318
Received 2 October 2023; Received in revised form 15 December 2023; Accepted 4 January 2024
Available online 11 January 2024

impurities (e.g., Al isomorphous substitution) (Li et al., 2016), which result in the generation of vacancy defects in the structure, thereby showing different interfacial reactivities for heavy metal(loid) immobilization.

In general, vacancy defects in iron (oxyhydr)oxides arise from a deviation in the perfect structure (Ilton et al., 2020), and can be divided into two types, i.e., either oxygen vacancies or Fe vacancies. These vacancy defects are usually characterized as an excess of hydroxyl groups relative to the theoretical formula of (α-$Fe_{2-y/3}O_{3-y}(OH)_y$) (Cornell and Schwertmann, 2003). A growing body of studies demonstrated that vacancy defects have considerable influence on the reactivity of iron (oxyhydr)oxides (Bylaska et al., 2019; Fang et al., 2023; Notini et al., 2019, 2018). For example, Scherer and co-authors employed ^{57}Fe Mössbauer spectroscopy and synchrotron X-ray absorption and magnetic circular dichroism spectroscopies to experimentally demonstrate the important contribution of Fe vacancy defects in goethite to accelerating Fe(II)–Fe(III) oxide electron transfer (Notini et al., 2018). Interestingly, they further found that vacancy defects also play an essential role in promoting microbial reduction of goethite (Notini et al., 2019). Chi et al. observed that fungi had a robust defect engineering strategy to regulate the vacancy defects (e.g., oxygen vacancies) in iron oxide nanoparticles (Chi et al., 2022), thereby modulating the intrinsic peroxidase-like activity of the iron minerals through decreasing the catalytic activity of poorly-crystalline ferrihydrite, but promoting that of well-crystalline hematite. In our previous work, we combined batch kinetic experiments and density functional theory (DFT) calculations to reveal that vacancy defects in minerals (e.g., manganese oxides) have a considerable effect on the redox transformation of arsenite to arsenate by minerals (Hou et al., 2017, 2016). Specifically, we showed that the higher the concentration of vacancy defects in manganese oxides is, the faster As(III) was oxidized to As(V). Moreover, the vacancy defects were found to affect the unit cell parameters of iron oxyhydroxides (Schwertmann et al., 1985).

Fe-bearing minerals have been reported to be a sink for a series for heavy metals (Bargar et al., 2004; Liu et al., 2015; Noerpel et al., 2016; Roberts et al., 2017). Therefore, the interfacial reaction behavior of different heavy metal(loid)s on hematite surfaces has been extensively studied in previous work. For example, Yan et al. (2020) investigated the hematite facet-dependent adsorption mechanisms for the arsenic oxyanions (As(III) and As(V)) using multiple spectroscopic characterization techniques and DFT calculations. They found that monodentate mononuclear surface complexes of As(III/V) were formed on the {001} facet, while bidentate binuclear surface complexes appeared on the {110} and {214} facets. These different adsorption configurations were explained by the chemical diversity in surface active sites of the exposed lattice, which led to a different bonding strengths, thereby showing a different capacity for arsenic immobilization, i.e., {214} > {110} > {001}. Qiu et al. (2020) employed crystal truncation rod (CTR) X-ray diffraction and density functional theory (DFT) calculations to reveal that the cation Pb(II) selectively adsorbs on the (1 $\bar{1}$ 02) hematite surface, i.e., the cation Pb(II) adsorbs energetically favored on edge-sharing surface sites of hematite. These results demonstrate that any slight changes in the hematite surfaces could alter the adsorption configuration of heavy metal(loid)s, thereby affecting their migration and fate in soils and sediments controlled by iron minerals. We hypothesized that vacancy defects in the hematite structure may also influence the adsorption configuration of heavy metal(loid)s on hematite. Until now, molecular-level understanding of how the vacancy defects affect heavy metal(loid) immobilization by hematite is missing, although there is evidence that defects exist in the structure of hematite in nature.

In the present study, hematite samples with tunable vacancy defects were obtained by a ball-milling treatment of well-crystallized hematite through variation of the ball-milling time. The adsorption capacities of the defective hematite samples for the two typical cation- and oxyanion-type heavy metal(loid)s lead [Pb(II)] and arsenate [As(V)] were evaluated. X-ray absorption spectroscopy (XAS) and theoretical calculations of the partial density of states (PDOS) and crystal orbital Hamilton population (COHP) analysis were employed to investigate the effect of vacancy defects on the coordination environments and bonding strengths of these two heavy metal(loid)s on hematite. The objectives of this study were (1) to investigate the characteristics of vacancy defects in hematite structure; (2) to evaluate the effects of vacancies on Pb(II) and As(V) adsorption by hematite; and (3) to reveal the underlying mechanisms of how vacancy defects influence Pb(II) and As(V) immobilization.

2. Experimental section

2.1. Sample preparation

Hematite was synthesized based on previous literature (Burstein, 1992). Briefly, 500 mL of $Fe(NO_3)_3$ (0.1 M) and 300 mL of KOH (1 M) solutions were heated separately to 90 °C in an oven and subsequently mixed in a 1 L polypropylene (PP) beaker under continuous magnetic stirring. 50 mL $NaHCO_3$ (1 M) was added and the resulting solution was maintained in the oven at 90 °C for 4 days. Afterwards, the precipitate was filtered and washed with ultrapure water until the conductivity was lower than 10 μS cm^{-1}. The hematite powders were calcined at 600 °C in a muffle furnace for 5 h to obtain the well-crystallized and defect-free hematite sample (denoted as DFH). Ball-milling was shown to be a suitable approach to produce vacancy defects in iron oxides (Ciotonea et al., 2017; Madsen et al., 2009; Manas and Alok, 2008). Thus, the DFH sample was treated using ball-milling at relatively short and long times of 4 and 10 h to prepare defect-poor hematite (denoted as DPH) and defect-rich hematite (denoted as DRH), respectively.

2.2. Sample characterization

The mineral phase, morphology, specific surface area, surface element species, and charge characteristics of the defective hematite samples were characterized using X-ray diffraction (XRD), scanning electron microscopy (SEM), transmission electron microscopy-energy dispersion spectrum (EDS) mapping, N_2 adsorption/desorption isotherm analysis, X-ray photoelectron spectroscopy (XPS), and zeta potential measurements, respectively. Positron annihilation lifetime (PAL) spectroscopy data were collected at the University of Science and Technology of China (USTC). XAS measurements at the Fe K-edge of hematite, As K-edge of As(V)-adsorbed hematite, and Pb L_{III}-edge of Pb (II)-adsorbed hematite samples were carried out at the 1W1B beam line of the Beijing Synchrotron Radiation Facility (BSRF, China). The Extended X-ray Absorption Fine Structure (EXAFS) data were acquired from −200 to 800 eV with three to five spectra to reduce the noise. Detailed information on the characterization is presented in Text S1 (Supplementary Materials).

2.3. As(V) and Pb(II) adsorption experiments

As(V) and Pb(II) adsorption on hematite samples was evaluated using batch experiments at pH 6.0. First, 0.040 g hematite powder was added to 200 mL ultrapure water to obtain 0.2 g L^{-1} suspensions. The suspension pH was adjusted to the target value of 6.0 using HNO_3 (0.1 M) and NaOH (0.1 M), and maintained for several hours until the solution pH was stable. High-purity N_2 was introduced into the solution to prevent any influence of CO_2 from the atmosphere. Subsequently, 10 mL of the suspensions were transferred into 50 mL centrifuge tubes. $Na_3AsO_4{\cdot}12H_2O$ and $Pb(NO_3)_2$ salts were used to prepare As(V) and Pb(II) stock solutions. The As(V) and Pb(II) working solutions were obtained through diluting their corresponding stock solutions. For As(V) adsorption experiments, the initial As(V) concentrations varied from 0 to 26.7 μM, while for Pb(II), its initial concentrations were set in the range of 0–57.9 μM. Before the adsorption experiments, a series of Pb(II)

or As(V) solutions (10 mL) were added to centrifuge tubes (containing 10 mL of 0.2 g L^{-1} suspensions), which were subsequently transferred into a thermostatic shaker (280 rpm) at 25 °C. To maintain the solution pH stable, we adjusted the pH value several times during the adsorption processes. All adsorption experiments were performed in triplicates. The experiments for determining the effect of pH on As(V) and Pb(II) adsorption were carried out in a series of 50 mL centrifuge tubes. The initial As(V) and Pb(II) concentrations were set as 53.4 and 19 μM, respectively. The hematite concentration was 0.2 g L^{-1}. The pH of the suspension was adjusted to pH 4.0, 5.0, and 6.0. After 24 h, the suspensions were centrifuged at 10,000 rpm for 10 min, and filtered through a 0.22-μm filter membrane. The residual lead concentrations in solution were quantified using atomic absorption spectrometry (AAS). Before the measurement of Pb, the solution was acidified with 1% HNO_3. The residual arsenic was quantified using an atomic fluorescence spectrometer (AFS-9700). The detailed procedure of total As quantification is shown in our previous work (Zheng et al., 2023).

2.4. Density functional theory (DFT) calculation

DFT calculations were used to theoretically investigate the underlying effects of vacancy defects in the hematite structure on arsenate and lead adsorption using the Vienna Ab-initio Simulation Package (VASP). The $H_2AsO_4^-$ and Pb^{2+} ions were employed as As(V) and Pb(II) species for performing DFT calculations, respectively, because they are the predominant species at pH 6 (the pH used in the adsorption experiments). The unit cell parameters used in this study are a = b = 5.04, c = 13.75 Å and α = β = 90°, γ = 120°. A {012} facet with four atomic layers of Fe and more than 15 Å of vacuum region along the *y* direction was constructed. The (012) surface was cleaved from the optimized bulk structure of a 2 × 1 × 1 supercell. Figure S1 exhibits the hydroxylated hematite surface with one Fe vacancy. The formula of adsorption energy (E_{ads}) was described as follows (Hou et al., 2017, 2016). $E_{ads} = E_{molecule + slab} - E_{slab} - E_{molecule}$, where E_{slab} and $E_{molecule}$ represent the energy of the slab and the heavy metal ion to be adsorbed, respectively. $E_{molecule + slab}$ is the total energy of the slab with the adsorbed heavy metal ion. The electronic structure of hematite after adsorption was investigated using the LOBSTER 4.1 program (Tang et al., 2023; Yan et al., 2021, 2020). The partial density of states (PDOS) and crystal orbital Hamilton population (COHP) analysis were carried out to investigate the bonding chemistry of As(V) and Pb(II) adsorption on hematite. Detailed parameters for performing DFT calculations are shown in Text S2.

3. Results and discussion

3.1. Bulk characterization of hematite

Fig. 1a shows the XRD patterns of DFH, DPH, and DRH samples. All studied solids could be indexed to the hematite structure, and no impurities of other iron oxides were observed in the XRD patterns.

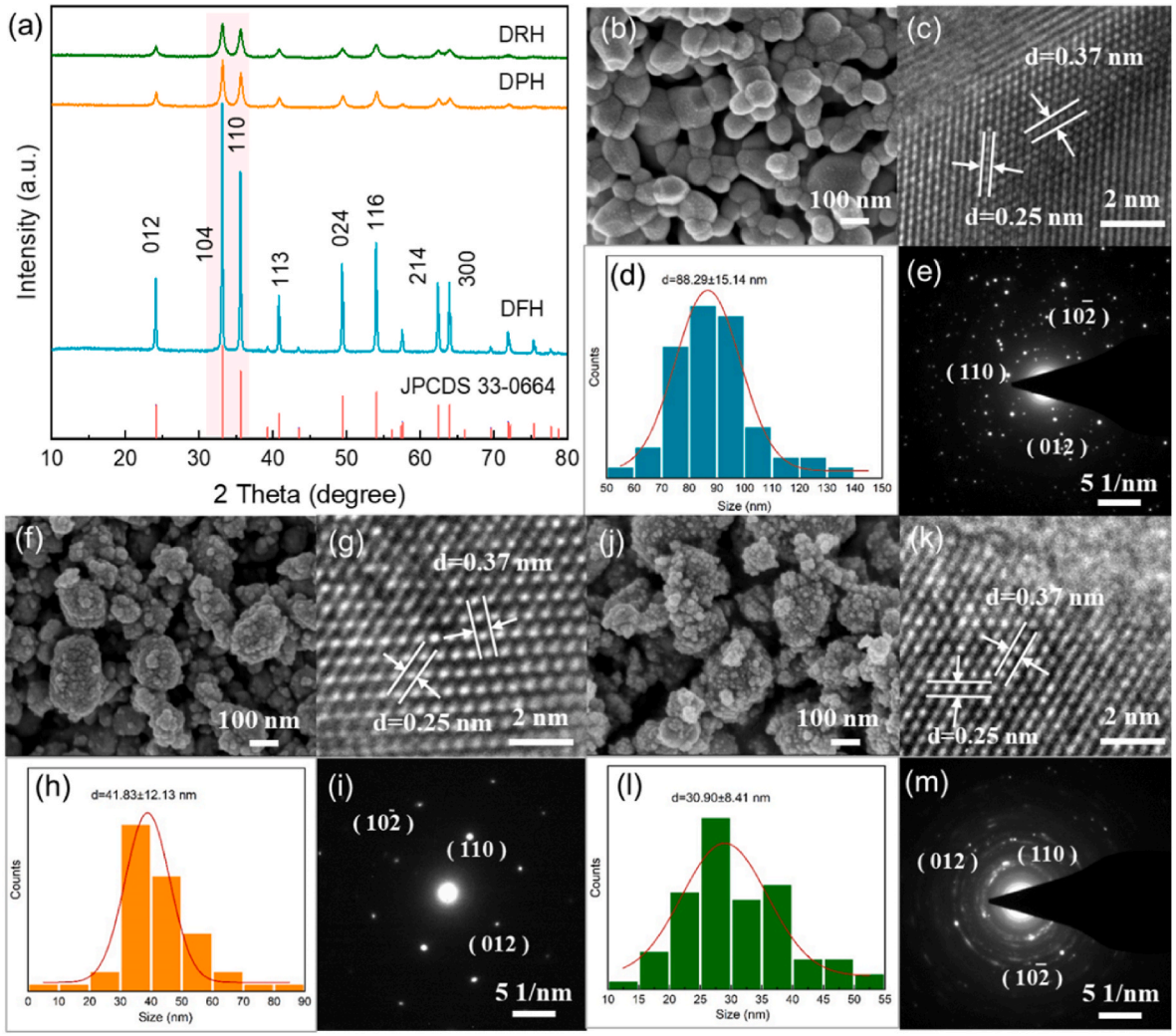

Fig. 1. XRD patterns (a), SEM (b, f, j), HRTEM (c, g, and k) images, histograms distribution of particles (d, h, and l), and SAED patterns (e, i, and m) of hematite samples with ball milling of 0 h (labeled as DFH), 4 h (labeled as DPH), and 12 h (labeled as DRH), respectively.

Compared to the hematite sample before calcination, the peak intensities of XRD patterns in the DFH sample became very strong, indicating that the calcination treatment increased the crystallinity of hematite and removed the defects in the structure (Figure S2a). After ball milling for 4 h, the reflection intensities of the XRD reflections for the DPH sample decreased compared to these of the DFH sample. When increasing the ball milling time to 12 h, the reflection intensities of the XRD patterns in the hematite sample (DRH) decreased further. This demonstrated that ball milling caused a decrease in the crystallinity of hematite, which was beneficial to generate vacancy defects (e.g., Fe vacancies). Moreover, we observed that the {104} and {110} diffraction signals in DPH and DRH samples shifted to higher angles compared to those in the DFH sample (Figure S2b). This phenomenon was also observed in previous work, which was assigned to the defects generated during the ball milling process (Manas and Alok, 2008). Moreover, the specific surface areas of DFH, DPH, and DRH samples, measured by fitting the N_2 adsorption curves through the Brunauer-Emmett-Teller (BET) model (Figure S3), were 7.32, 22.36, and 31.14 $m^2\ g^{-1}$, respectively.

SEM images revealed that the DFH sample showed a typical spherical-like morphology assembled by regular particles (Fig. 1b). After ball milling, the solids had many fragmented and irregular particles (Fig. 1f and j). The distribution of particle sizes in the three different hematite samples were determined based on the SEM images. As shown in Fig. 1d, the predominant particle size in the DFH sample was 70–100 nm, which was larger than those in DPH (30–60 nm) and DRH (20–40 nm) samples (Fig. 1h and i). The average particle sizes of DFH, DPH, and DRH samples, calculated based on their corresponding histograms, were 88.3, 41.8, and 30.5 nm, respectively. This result revealed that ball milling considerably decreased the particle sizes in hematite. The specific surface areas of hematite samples were obtained by measuring N_2 adsorption curves, where more N_2 adsorbed on hematite corresponds to a larger surface area as calculated through the BET model. We found that the DRH sample that has a small particle size showed a relatively high N_2 adsorption volume compared to DFH and DPH samples (Figure S3), explaining why the DRH sample exhibited the highest surface area compared to the DPH and DFH samples. The HRTEM images showed that three hematite samples had identical lattice fringes of 0.25 and 0.37 nm (Fig. 1c, g, and 1k), which were assigned to the {110} and {012} facets, respectively, as evidenced by their corresponding SAED patterns (Fig. 1e, i, and 1m).

The relative atom ratios of Fe to O in the three different hematite samples were calculated using TEM-EDS mapping. Figure S4 exhibits the distribution of iron and oxygen and their corresponding contents in the three hematite samples. In principle, the stoichiometry ratio of Fe to O in a perfect hematite structure should be 0.67 according to its chemical formula of α-Fe_2O_3 (Fe/O = 2/3), therefore, the relative Fe/O atomic ratio in hematite could qualitatively reflect the possible type of defects. For the DFH sample, the calculated Fe/O ratio was 0.55 (Figure S4). After ball milling, the calculated Fe/O ratios in DPH and DRH samples further decreased to 0.48 and 0.43, respectively, indicating that the ball milling treatment produced more Fe vacancies in the hematite structure (Chakrabarti et al., 2008; Zhang et al., 2003). It should be noted that because EDS-mapping analysis is a qualitative or semi-quantitative tool,

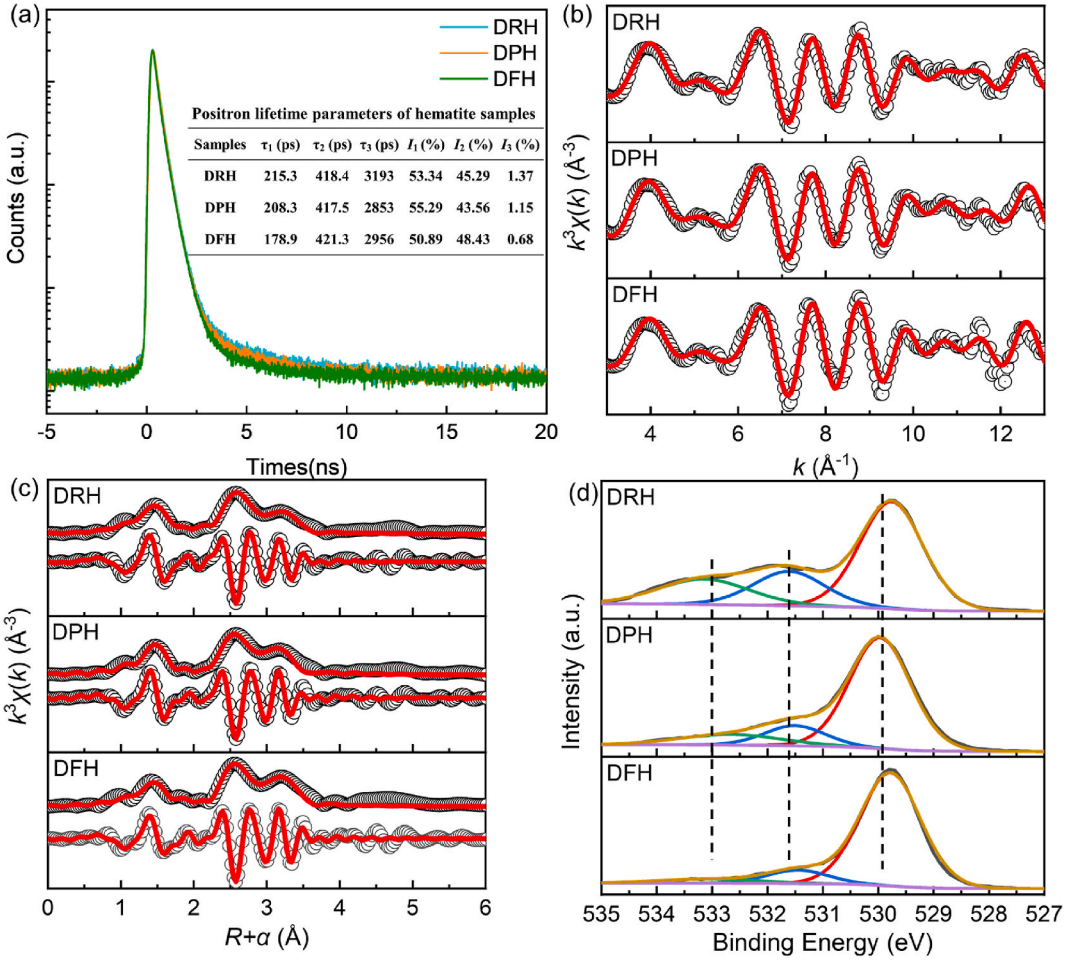

Fig. 2. Peak-normalized positron annihilation lifetime spectra (a), the Fourier transformed *k* space (b) and *R* space (c) profiles of Fe K-edge EXAFS spectra, and the O1s XPS spectra (d) of DFH, DPH, and DRH samples.

the defect characteristics of hematite still needs to be further confirmed using other characterization techniques (see section 3.2).

3.2. Defect characteristics in hematite

Positron annihilation lifetime (PAL) spectroscopy is a sensitive approach for detecting vacancy defects in minerals, which has also been employed to analyze vacancies in iron oxides (Bocquet and Hill, 1995). Fig. 2a illustrates the peak-normalized PAL spectra of our hematite samples. The PAL spectra of the three samples showed a slight difference in positron annihilation life, indicating that the three hematite samples had different characteristics regarding their vacancy defects. The PAL spectra could be well decomposed into three lifetime components: τ_1, τ_2, and τ_3 (insert in Fig. 2a). The longest lifetime component τ_3 (~3 ns) was assigned to the pick-off annihilation of ortho-positronium (o-Ps) inside large voids in the mineral materials.[30,31] The medium lifetime component τ_2 (411.7–421.3 ps) corresponded to the positron annihilation in large-size defects (e.g., vacancy clusters), while the shortest lifetime component τ_1 (178.9–210.7 ps) could be attributed to the defect-free bulk regions and/or tiny vacancies (Dutta et al., 2006; Kong et al., 2011; Liu et al., 2009). Thus, the lifetime components τ_1 and τ_2 can be used to explain the existence of defects. As shown in the Table inserted in Fig. 2a, the fraction I_3 in the three hematite samples was lower than I_1 and I_2. For the DPH sample, its I_1 and I_2 values were 55.29% and 43.56%, respectively, while that for the DRH sample were 45.85% and 52.99%, respectively. This result demonstrated that there were defects in the DPH and DRH samples. Although the vacancy defect concentration in the DFH sample was extremely low due to the calcination treatment, it was still detectable by PAL characterization. This result suggested that PAL analysis is a sensitive tool to probe the defects. In principle, vacancies in the hematite structure must be negatively charged or neutral for trapping positrons. Therefore, the defects in our hematite samples most likely existed in the form of Fe vacancies.

To further evaluate the vacancy defect type in hematite samples, EXAFS analysis was used to investigate the coordination of Fe, i.e., the Fe–O and Fe–Fe bonding environments. Fig. 2b and S5 shows the Fe K-edge EXAFS spectra of the three hematite samples. A peak at ~5.5 $Å^{-1}$, which is typical of crystalline Fe (oxyhydr)oxides, was observed in the Fe K-edge EXAFS spectrum of the DFH sample (Toner et al., 2009; Van Genuchten et al., 2012). The Fe K-edge EXAFS spectrum of DPH and DRH samples was similar as that of DFH sample. This indicated that ball milling did not alter the basic structure of hematite. The Fourier transformed (FT) EXAFS spectra of the hematite samples are shown in Fig. 2c. There were three relatively strong peaks in the FT EXAFS spectra of the hematite samples. A strong peak appeared at approximately ~1.5 Å, corresponding to the first shell of Fe–O coordination, while two other strong peaks appeared at approximately 2.6 and 3.2 Å (Li et al., 2016). Table S1 presents the fitting parameters of FT EXAFS spectra using the Artemis software. The total coordination number of the Fe–O shell ($CN_{Fe–O}$) in the DFH sample (5.86) showed no obvious difference compared to that of the DPH (6.22) and the DRH (6.12) samples. Moreover, we set the CN of face-sharing (Fe–Fe_1) ($CN_{Fe–Fe1}$) as floating value. The CN values of edge-sharing (Fe–Fe_2) ($CN_{Fe–Fe2}$) and corner-sharing Fe–Fe (Fe–Fe_3 and Fe–Fe_4) ($CN_{Fe–Fe3}$ and $CN_{Fe–Fe4}$) were set as linear change with the $CN_{Fe–Fe1}$ based on the reported treatment approach (Van Genuchten et al., 2012). As shown in Table S2, the fitted $CN_{Fe–Fe1}$ value for DFH was 1.0, while those in DPH and DRH samples decreased to 0.81 and 0.75, respectively. Correspondingly, the $CN_{Fe–Fe1\text{-}2}$, $CN_{Fe–Fe3}$, and $CN_{Fe–Fe4}$ in DPH and DRH samples also decreased compared to those in DFH sample. In general, an octahedral [FeO_6] unit shows a theoretical $CN_{Fe–O}$ value of 6.0, i.e., one Fe atom is surrounded by six oxygen atom. If oxygen vacancies exist in the hematite structure, the $CN_{Fe–O}$ value must decrease. Correspondingly, $CN_{Fe–Fe}$ will also decrease if Fe vacancies exist in the hematite structure. Therefore, the coordination information obtained from EXAFS analyses can be used to evaluate the distribution of Fe and O in the structure of iron oxides. In our study, the $CN_{Fe–O}$ values for the three hematite samples did not change obviously, suggesting that oxygen vacancies were not the primary defect type in the hematite structure. However, the total $CN_{Fe–Fe}$ values in the three hematite samples showed an evident difference, with the one in the DRH sample being the lowest one, followed by the values obtained for the DPH and the DFH samples. These low $CN_{Fe–Fe}$ values indicated that Fe vacancies were the primary defect type in the structure of DPH and DRH samples, in agreement with our PAL analysis.

The surface sensitive technique XPS was employed further to confirm the presence of Fe vacancy defects. In general, the presence of Fe vacancies at the surface of hematite would expose more oxygen atoms adjacent to the Fe vacancies, causing adsorption of protons from solution to maintain the charge balance, thus forming more hydroxyl species in the surface structure of hematite. Fig. 2d illustrates the profiles of O1s XPS spectra of our three different hematite samples. All O1s XPS spectra could be well deconvoluted into three peaks at ~529.8, ~530.1, and ~529.8 eV, respectively (Table S2). The binding energy peak at ~530.1 eV corresponded to the lattice oxygen species (O_{latt}) in hematite (Santos et al., 2010), while those at ~531.7 and ~533.2 eV were attributed to the hydroxyl oxygen ($O_{–OH}$) and water-molecule oxygen (O_{H2O}) species, respectively (Jönsson and Sherman, 2008; Santos et al., 2010). The evolution of the $O_{–OH}$ concentration in the different samples is presented in Table S2. The DRH sample showed the highest ratio of $O_{–OH}/O_{latt}$ (5.88), followed by the DRH (4.35) and the DFH (2.78) samples, demonstrating that the DRH sample possessed a relatively high content of Fe vacancies, which was consistent with the results from PAL, EDS-mapping, and Fe K-edge EXAFS.

3.3. Arsenate and lead adsorption on defective hematite

As(V) and Pb(II) represent typical oxyanion- and cation-type heavy metal(loid)s, respectively, which are commonly found in polluted soils and groundwaters. In this study, the As(V) and Pb(II) adsorption capacities of defective hematite samples were examined to investigate the underlying effect of Fe vacancies on the mobility of arsenic and lead in natural environments. Considering that the three hematite samples had different surface areas, the adsorption capacities for As(V) and Pb(II) were normalized by dividing through their corresponding specific surface areas. Fig. 3a and b shows the surface area-normalized adsorption isotherms of As(V) and Pb(II), respectively. Langmuir and Freundlich models were used to fit the As(V) and Pb(II) adsorption isotherms (Fig. 3 and S6). The surface area-normalized As(V) and Pb(II) adsorption isotherms could be well described using the Langmuir model, as evidenced by its relatively high R^2 value compared to that of the Freundlich model (Table S3). Therefore, the maximum amounts of adsorbed As(V) and Pb (II) on defective hematite samples were calculated using the Langmuir model. Increasing the Fe vacancy defects led to an increase in As(V) adsorption, i.e., the maximum amount of As(V) adsorption by the DPH and DRH samples increased from 1.86 (for the DFH sample) to 2.02 and 2.30 μmol m^{-2}, respectively (Fig. 3c). This result indicated that the presence of defects in naturally occurring iron oxides could promote arsenic immobilization, thus possibly reducing the risk of arsenic migration. On the contrary, the increase of vacancy defects was lowering Pb(II) adsorption on hematite, i.e., the DRH sample with the highest amount of Fe vacancy defects showed the lowest Pb(II) adsorption (5.04 μmol m^{-2}), followed by the DPH (9.80 μmol m^{-2}) and the DFH (24.74 μmol m^{-2}) samples (Fig. 3c). We also evaluated As(V) and Pb(II) adsorption on the three hematite samples at lower pH values of 4.0 and 5.0. As shown in Figure S7, As(V) adsorption on the three hematite samples increased with decreasing solution pH, while adsorption for Pb (II) decreased. A similar effect was already observed in previous reports (Du et al., 2019, 2018; Xue et al., 2019). Although the solution pH had a significant effect on As(V) and Pb(II) adsorption, the amount of As(V) adsorbing on the DRH sample at a given pH was always higher than that on the DPH and DFH samples, while the amount of Pb(II) adsorbing on

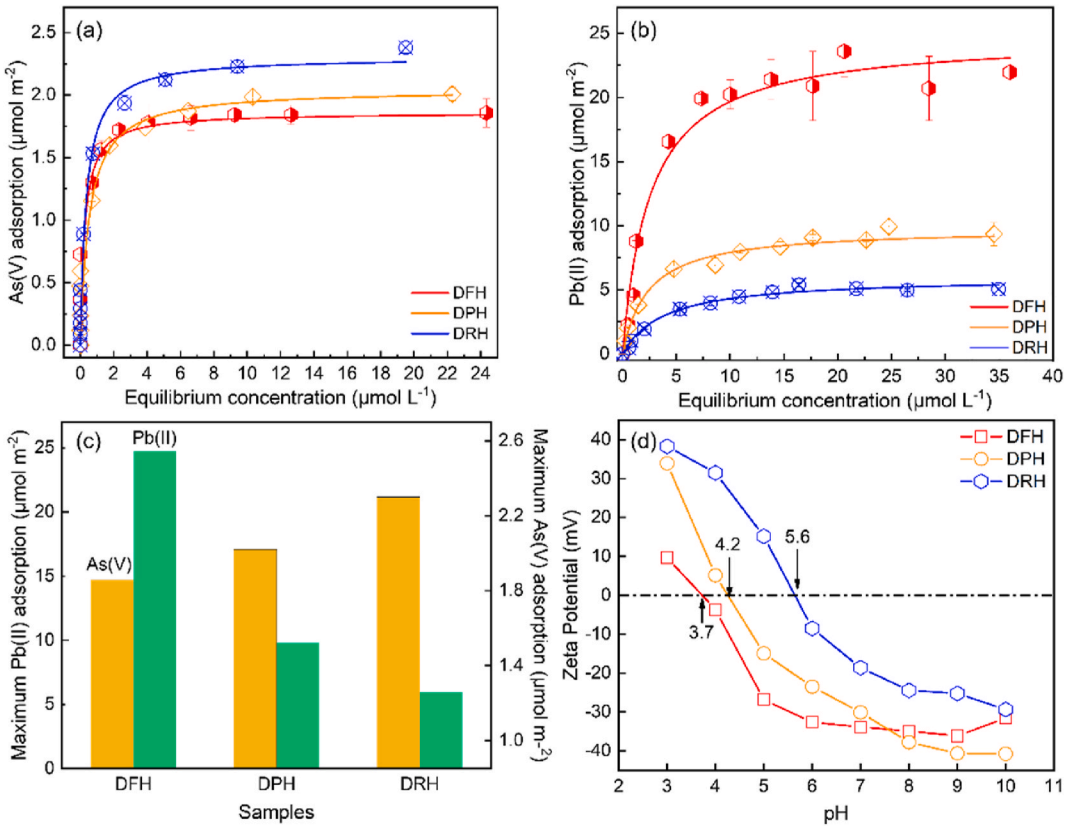

Fig. 3. Adsorption isotherms of three different hematite samples with different amounts of vacancy defects for As(V) (a) and Pb(II) (b) at pH 6.0 and their corresponding maximum adsorption amount (c) and Zeta potential values (d) for the three different hematite samples. A Langmuir model was used to fit the adsorption data. All adsorption experiments were performed three times.

the DRH sample was always the lowest one among three hematite samples. This is the first time where the contrasting influences of Fe vacancy defects on As(V) and Pb(II) adsorption were observed experimentally, which aids in understanding the fate and transport of these two toxic heavy metal(loid)s in polluted environments.

3.4. The underlying mechanisms of vacancy defect effects on As(V) and Pb(II) adsorption

3.4.1. The effect of morphology, phase structure, and surface charge

The key question resulting from our results is why the Fe vacancy defects show opposite influences on As(V) and Pb(II) sorption. It is widely accepted that several factors, including mineral surface area, phase structure, morphology, and exposed lattice facets, influence or even control heavy metal adsorption on minerals. In this study, the adsorption capacities of hematite samples for As(V) and Pb(II) were normalized by their corresponding specific surface areas. We found that the efficiency for As(V) and Pb(II) adsorption did not linearly increase with increasing specific surface area of hematite. Previous studies have shown that the exposed lattice facet exhibited a strong selectivity for the adsorption of certain heavy metals due to the differences in surface energy (Yan et al., 2021, 2020). For example, the {001} facet of hematite was regarded as an inactive lattice facet compared to the two other facets {214} and {014} (Yan et al., 2021, 2020). In this study, all hematite samples had the same exposed facets of {012} and {110}. Although the particle size and roughness of our three samples were different, they still showed a spherical-like morphology with the same phase structure of hematite, as evidenced by TEM and XRD analysis.

It is well known that the surface charge of iron (oxyhydr)oxides has important effects on heavy metal adsorption. To find out whether the Fe vacancy defects affected the surface charge characteristics of hematite particles, we analyzed the zeta potentials of our three hematite samples. Fig. 3d shows the zeta potential profiles of the different samples as a function of pH. For the DFH sample, its isoelectric point (IEP) appeared to be at pH 3.7. Increasing the Fe vacancy defects led to an increase in the IEP of hematite samples, with IEP values of 4.2 and 5.6 for DPH and DRH samples, respectively. This result indicated that Fe vacancies had a considerable influence on the surface charge of the hematite particles. Remarkably, the zeta potential of the DFH sample at pH 6, i.e., the pH value used in the batch adsorption experiments of this study, was −32.8 mV, which should be beneficial to the adsorption of positively charged Pb(II) ions due to the electrostatic attraction, and disadvantageous for adsorption of the negatively charged As(V) species. Our data showed that the presence of Fe vacancies led to an increase of the zeta potential values (they became less negative). Compared to the DFH sample, the zeta potential of the DPH and DRH samples at pH 6 changed to −23.8 and −8.4 mV, respectively. The decreasing attraction for cations and the increasing attraction for oxyanions for the series of hematite samples from DFH to DPH and to DRH is in agreement with the adsorption trends for Pb(II) and As(V) species.

3.4.2. Binding analysis of As(V) on defective hematite

As–K edge EXAFS data of As-adsorbed hematite samples was collected to reveal possible effects of vacancy defects on the coordination environment of As–Fe. Fig. 4a and b illustrate the As K-edge EXAFS spectra of the three samples and their corresponding Fourier-transformed radial distribution function (RDF) profiles. The fitting results of the coordination number (CN) and interatomic distance are presented in Table S4. The RDF profile of As(V)-adsorbed DFH sample had two predominant coordination shells of As–O and As–Fe bonds. In the As–O coordination shell, the As atom was surrounded by oxygen atoms at 1.69 Å with a CN of 3.6, which was assigned to the molecular

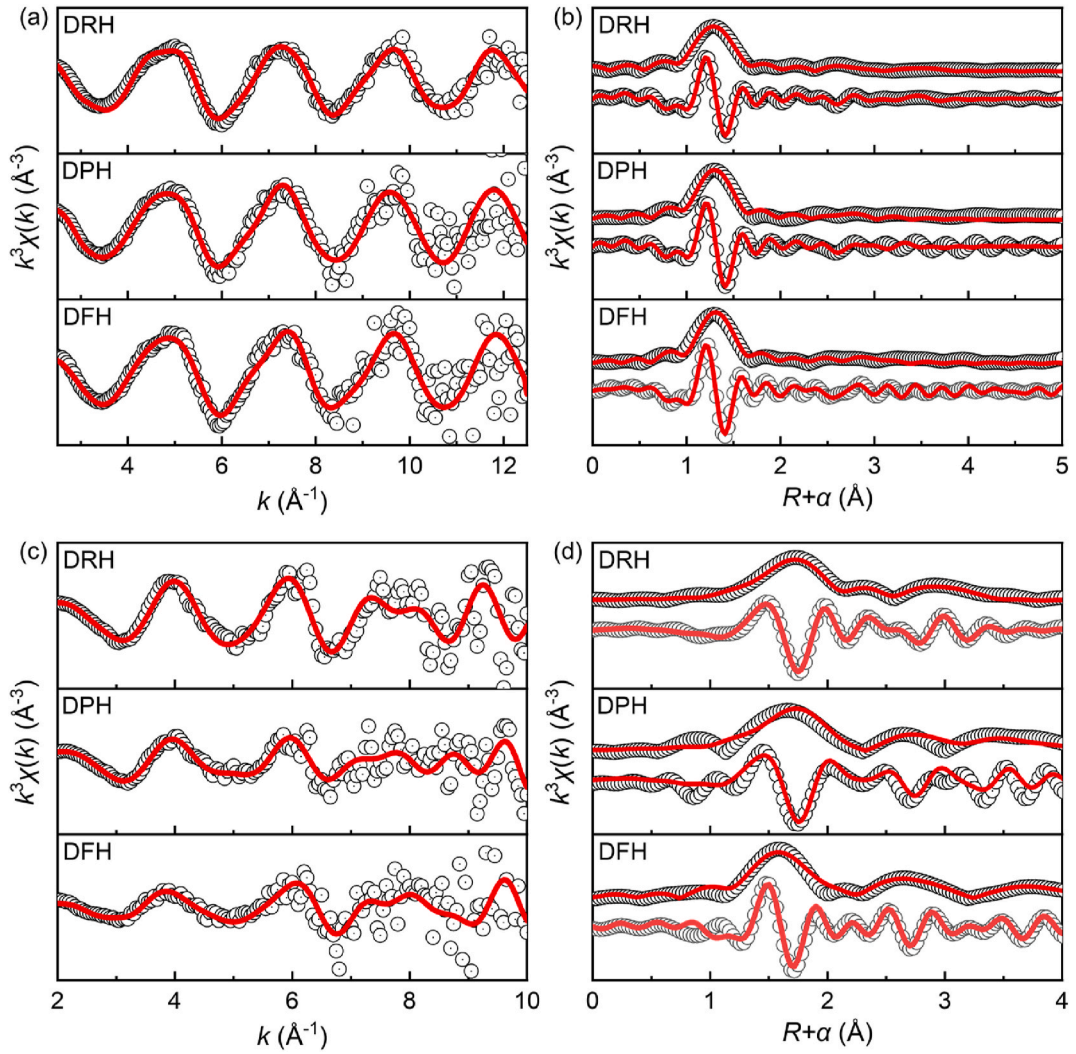

Fig. 4. As K-edge (a, b) and Pb-L_{III} edge (c, d) EXAFS data for As(V)- and Pb(II)-adsorbed hematite samples, respectively: (a, c) k^3-weighed EXAFS data and (b, d) corresponding Fourier-transformed radial distribution functions (including FT magnitude and imaginary part). White open circles and red solid lines represent the experimental and fitted data, respectively. (For interpretation of the references to colour in this figure legend, the reader is referred to the Web version of this article.)

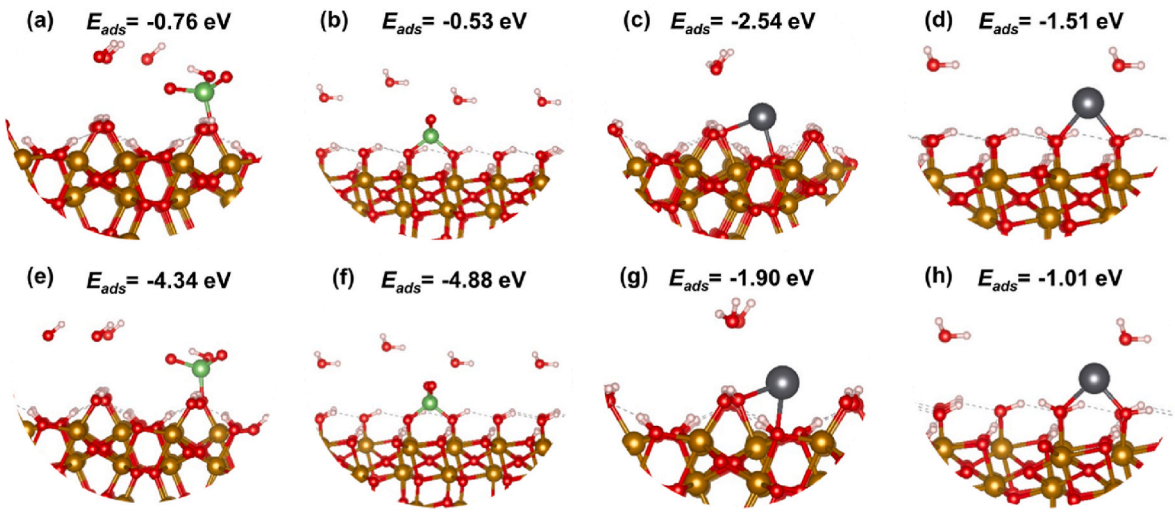

Fig. 5. Optimized structure of the complexes for As(V) ($H_2AsO_4^-$) (a, b, e, and f) and Pb(II) (c, d, g and h) adsorption on the surface of a hematite slab in the absence and in the presence of one Fe atom vacancy: White represents hydrogen atoms, green arsenic atoms, black stands for lead atoms, red for oxygen atoms, and luminous yellow represents Fe atoms. (For interpretation of the references to colour in this figure legend, the reader is referred to the Web version of this article.)

structure of an AsO_4 tetrahedron (Jönsson and Sherman, 2008; Wang et al., 2011). In the As–Fe coordination shell, the As atom was surrounded by Fe atoms at ~3.36 Å with a CN of 1.3, suggesting the formation of a monodentate mononuclear (^{1}V) complex (Mikutta and Kretzschmar, 2011; Yan et al., 2020). This was also confirmed by DFT calculations, i.e., the calculated As(V) reaction adsorption energy on a pristine hematite surface in the form of a ^{1}V complex model (−0.76 eV) was lower than that of a bidentate model (−0.53 eV) (Fig. 5a and b), suggesting that the formation of a ^{1}V complex is more favorable in defect-free hematite. Previous studies revealed an As–O–O scattering path in the RDF profile of an As(V)-adsorbed hematite sample (Liu et al., 2015; Van Genuchten et al., 2012). In the present study, we also observed such an As–O–O scattering path with a *R* value of 3.10 Å and a CN of 12.

The detailed chemical bonding between arsenate and hematite was elucidated by the analysis of partial density of states (PDOS) and crystal orbital Hamilton population (COHP) to further reveal the effect of Fe vacancies on arsenic adsorption (Yan et al., 2020). The overlap of Fe 3d and O 2p orbitals below the Fermi level was observed in the Fe–O bond (Fig. 6), suggesting that the electron sharing between Fe 3d and O 2p orbitals primarily contributed to the formation of new Fe–O bonds. Compared to the pristine hematite sample with adsorbed arsenate in the form of a ^{1}V model, a significant delocalization of electron density below the Fermi level occurred in the defective hematite with adsorbed arsenate in the form of a ^{2}C model, as evidenced by a decrease in its intensity of PDOS. This result indicated that the change of coordination from a ^{1}V to a ^{2}C model induced by Fe vacancies was beneficial to the decrease of their orbital energies to form stable As–O–Fe complexes. The value of -ICOHP could be used as an indicator of As(V) bonding strength(Yan et al., 2020). Fig. 6b, d, and 6f illustrate the -ICOHP plots of coordinated Fe–O bonds in As(V) complexes on the pristine hematite in a ^{1}V model and on the surface of defective hematite in a ^{2}C model, respectively. For As(V) adsorption on pristine hematite, the -ICOHP value for coordinated Fe_{20}–O_{88} bond was −2.364 eV. The -ICOHP values for coordinated Fe_{20}–O_{87} and Fe_{28}–O_{29} on defective hematite were −2.247 and −2.405 eV, respectively. Remarkably, the total -ICOHP value (−4.652 eV) for the coordinated Fe–O bond on defective hematite was larger than that on pristine hematite. This result clearly demonstrated that Fe vacancies promoted the bonding strength of As(V) on hematite, which was in agreement with our adsorption energy calculation and PDOS analysis.

3.4.3. Binding analysis of Pb(II) on defective hematite

We collected Pb-L_{III} edge EXAFS data hematite samples with adsorbed Pb(II) to illustrate the Pb–Fe coordination environment on defective hematite (Fig. 4c and d). Table S6 summarizes the Pb-L_{III} edge EXAFS fitting results of the CN and R values. The Pb–O distance (R_{Pb-O}) in Pb (II) adsorbed to the DFH sample was ~2.24 Å, which was significantly different from the R_{Pb-O} of aqueous Pb(II) (~2.5 Å) (Bargar et al., 1997; Noerpel et al., 2016), indicating that Pb(II) ions directly complex to the hematite surface. Moreover, our DFH sample with adsorbed Pb(II) showed two types Pb–Fe coordination environments. The Pb–Fe_1 distance (R_{Pb-Fe1}) at ~3.26 Å was attributed to an edge-sharing (ES) bidentate complex, whereas the Pb–Fe_2 distance (R_{Pb-Fe2}) at ~3.80 Å corresponded to Pb(II) adsorbed in a corner-sharing bidentate (CS) or a monodentate mononuclear complex (Liu et al., 2018; Noerpel et al., 2016; Qiu et al., 2020). However, according to our DFT calculation result, the formation of a bidentate Pb–Fe complex seems to be more favorable than that of a monodentate mononuclear complex, because we found that an initial monodentate mononuclear structure of Pb(II) adsorbed on hematite readily transformed to the bidentate structure after structure optimization (Figure S8). This result suggested that that R_{Pb-Fe2} at ~3.90 Å is possibly attributed to a corner-sharing bidentate model (Noerpel et al., 2016). DPH and DRH samples with adsorbed Pb (II) showed Pb-L_{III} edge EXAFS profiles similar to the profile for the DFH sample with adsorbed Pb(II). Remarkably, Fe vacancies in hematite lead to an obvious shift of R_{Pb-O} and Pb–Fe distances to higher values, i.e., compared to the Pb(II)-adsorbed DFH sample, the R_{Pb-O}, R_{Pb-Fe1}, and R_{Pb-Fe1} values of the DRH sample increased from 2.24, 3.26, and 3.80 Å to 2.31, 3.34, and 3.92 Å, respectively (Table S6). The increased bond length of Fe–Pb meant that the Pb ions showed relatively weak adsorption on defective hematite compared to sorption at defect-free hematite, which was lowering Pb adsorption and therefore Pb immobilization.

To confirm the adverse effect of Fe vacancies on Pb immobilization

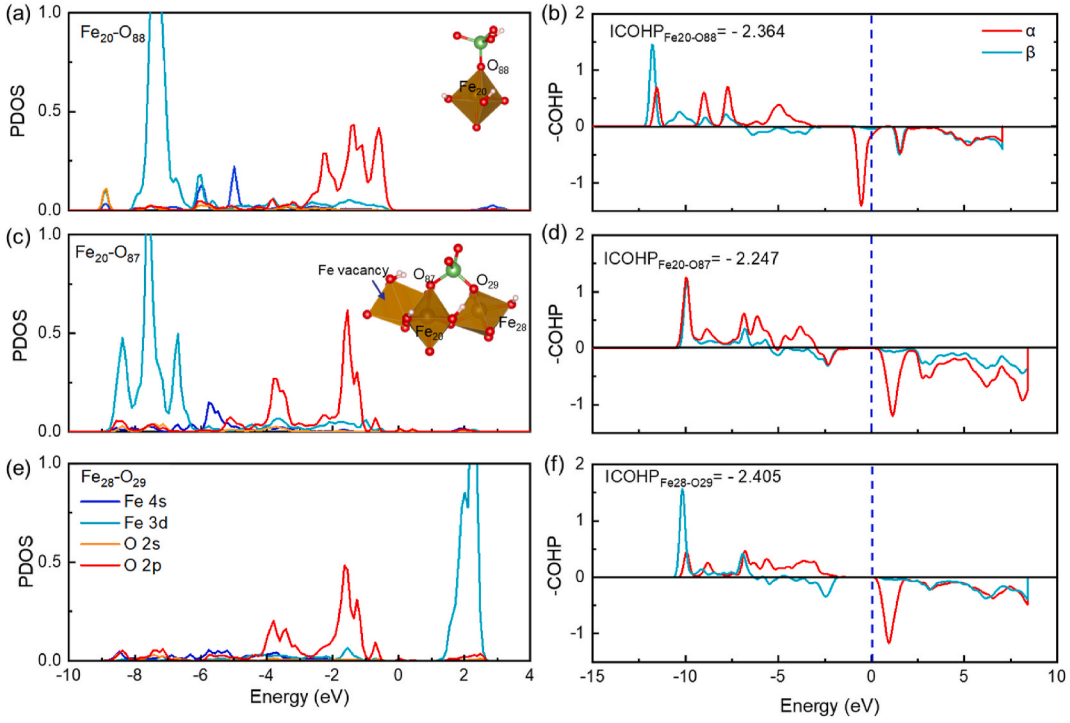

Fig. 6. PDOS (a, c, and e) and -COHP (b, d, and f) plots of the Fe–O bonds in As(V) complex on the perfect (a and b) and Fe vacancy hematite (c–f).

by hematite, we constructed edge-sharing (ES) and corner-sharing (CS) bidentate models based on the results of Pb-L_{III} edge EXAFS analysis for calculating Pb adsorption energies on the hematite surface in the presence and absence of one Fe vacancy. The constructed ES and CS bidentate models on hematite for Pb(II) adsorption are shown in Fig. 5c, d, 5g, and 5h. The calculated reaction adsorption energies of Pb(II) on pristine hematite surfaces in the ES and CS bidentate models were −3.63 and −1.51 eV, respectively (Fig. 5c and d). Compared to the pristine hematite, the reaction energies of Pb(II) adsorbed on the site adjacent to the Fe vacancy in the ES and CS bidentate models increased to −1.90 and −1.01 eV, respectively (Fig. 5g and h). This result combined with EXAFS analysis demonstrated that the presence of Fe vacancy decreased the affinity of hematite toward Pb(II), thereby leading to a decrease in Pb(II) immobilization.

The chemical bonding analysis for Pb(II) adsorption on defective hematite further revealed the results of EXAFS and DFT calculation. As shown in Fig. 7a and b, the Pb (6s), Pb (6p), O_{49} (2p), and O_{14} (2p) orbitals mainly contributed to the conduction band (0–10 eV) and upper valence band (−10–0 eV) after Pb(II) adsorption on hematite in a ES bidentate model. However, compared to pristine hematite with adsorbed Pb(II) (Fig. 7a), the intensity of the Pb (6s) orbital in the PDOS of defective hematite with adsorbed Pb(II) was observed to increase and that for Pb (6p) decreased (Fig. 7c). This result indicated that Fe vacancy affected the delocalization of electron density between Pb and O atom pairs. Moreover, the bonding behaviors of Pb and O on hematite differed in the ES and CS bidentate models. There were two main overlaps of PDOS for the Pb–O bonds after Pb(II) adsorption on hematite in a CS bidentate model, i.e., the interaction between Pb (6s) and O (2p) and the interaction between Pb(5d) and O (2s) orbitals (Fig. 7c and d), suggesting that the hybridization of Pb (6s) with the O (2p) orbital and Pb (5d) with the O (2s) simultaneously contributed to the formation of new Pb–O bonds on hematite. Remarkably, the intensity of Pb (5d) and O (2s) orbitals for the PDOS of Pb(II) adsorbed on hematite with the presence of one Fe vacancy became stronger compared to that of Pb(II) adsorbed to pristine hematite. This result indicated that the Fe vacancy in hematite increased the localization of electron density, thereby reducing the stability of the Pb–O–Fe complex. Fig. 7e–l illustrate the COHP analysis for the coordinated Pb–O bond in the ES and CS bidentate models. For the CS bidentate model, the ICOHP values of Pb_1–O_{14} and Pb_1–O_{49} bonds on pristine hematite were −1.619 and −1.226 eV (Fig. 7b and c), respectively, while those for the Pb_1–O_{14} and Pb_1–O_{40} bonds on hematite with one Fe vacancy changed to −1.457 and −1.349 eV (Fig. 7e and f), respectively. The total ICOHP value (−2.845 eV) of Pb–O bond on pristine hematite was lower than that on hematite with one Fe vacancy (−2.805 eV) (Table S7), suggesting that the bonding strength of Pb on defect-free hematite surface was stronger than that on defective hematite. The trends of changes of bonding strength of Pb on hematite in a CS bidentate model was similar to that in an ES model, i.e., the total ICOHP value of the Pb–O bond on defective hematite shifted to a high value of −3.707 eV compared to that on pristine hematite (−3.844 eV) (Table S7 and Fig. 7h–f). To sum up, Fe vacancies in hematite considerably decreased the bonding strength of Pb(II), thus leading to a decrease in Pb (II) adsorption on defective hematite.

3.5. Environmental significance

Vacancy defects are known to be present in naturally occurring and experimentally synthesized iron (oxyhydr)oxides. For example, we revealed that poorly-crystalline iron minerals contain abundant vacancy defect clusters, which were made up by 10–20 atom deficiencies (Zheng et al., 2023). We also observed previously that iron minerals synthesized in the laboratory at a relatively short time scale (e.g., aging of only 1 day) possessed many Fe vacancies (Hou et al., 2022). Additionally, the vacancy defect sites in iron (oxyhydr)oxides were confirmed to be the "hotspots" for arsenic immobilization. For instance, the vacancy clusters controlled As(III) and As(V) adsorption by poorly-crystalline ferrihydrite, which exhibited a different adsorption behavior compared to well-crystalline hematite (Zheng et al., 2023). The results obtained herein demonstrate that even small changes on Fe minerals (e.g., the presence of surface defects) can influence the bonding strength of heavy

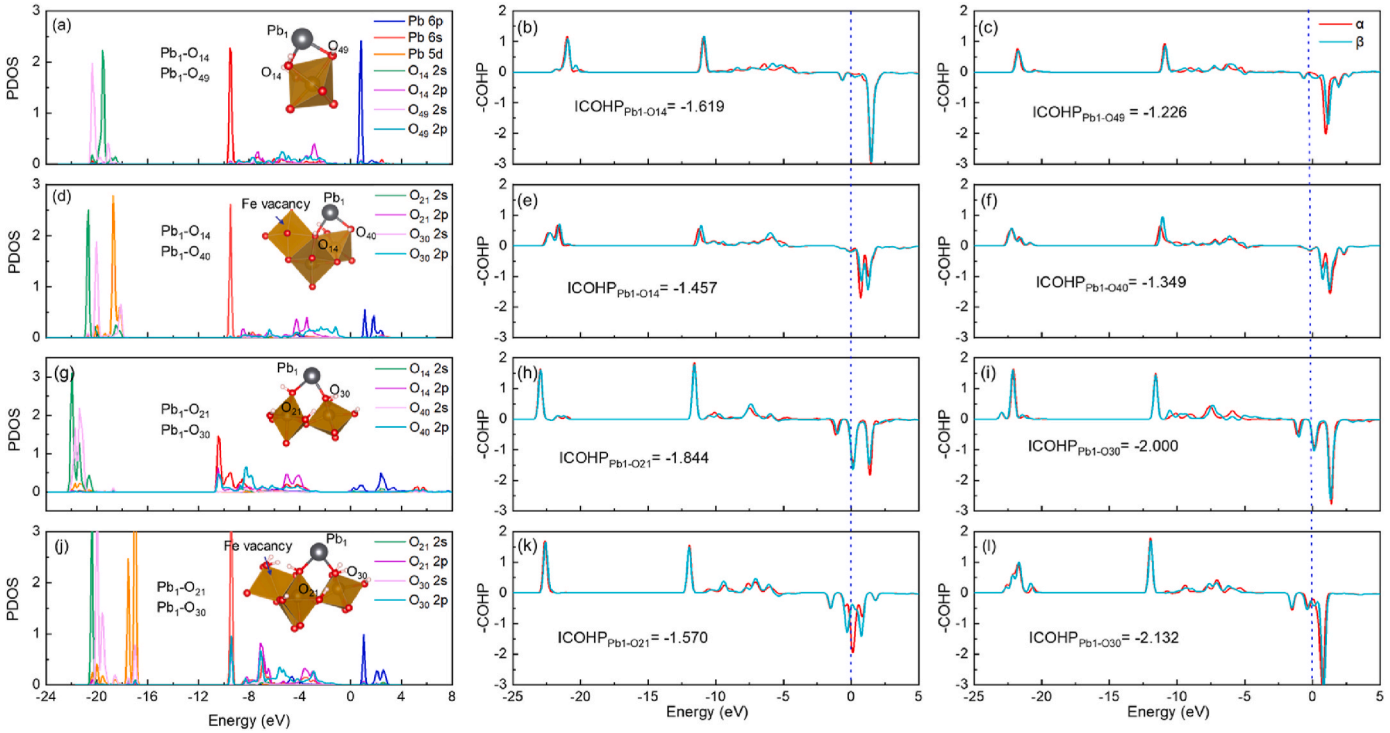

Fig. 7. PDOS (left) and -COHP (right) plots of coordinated Pb–O bonds in Pb(II) complexes on the hematite without and with one Fe vacancy in the bidentate edge-sharing (ES) (a–f) and bidentate corner-sharing (CS) (g–h) models.

metal(loid)s. Therefore, the effect of vacancies in the structure of Fe minerals for the migration of heavy metal(loid)s should be considered in future environmental studies. It should be noted that although other cation-type heavy metals such as Cd(II) and Cu(II) and oxyanion heavy metals such as Cr(VI), Sb(V), and V(V) show a similar charge as Pb(II) and As(V), respectively, their adsorption mechanisms on iron-bearing minerals still can be different. The effect of vacancies on the extent and mechanism of bonding of heavy metals needs to be further evaluated and discussed in future work for precisely understanding their migration and fate in natural environments controlled by iron-bearing minerals. Moreover, the results presented in this study are from laboratory-based studies, but not from actual contaminated environments. Further studies require to consider the real environment conditions such as co-existing ions, natural organic matters, and bacteria for evaluating the coupling effects of vacancies in iron-bearing minerals and the environment conditions on the migration of heavy metal(loid)s.

4. Conclusions

In summary, hematite samples with different defect concentrations were synthesized through ball milling of well-crystallized hematite via changing the ball milling time. The spectroscopic characterization using XAS, PAL, and XPS revealed that Fe vacancies were the primary defect type in the hematite structure. Batch adsorption experiments demonstrated that Fe vacancy defects had an opposite effect on Pb(II) and As(V) adsorption on hematite, i.e., increasing Fe vacancies led to an increase in As(V) adsorption, while resulting in an obvious decrease in Pb(II) adsorption. Fe vacancies increased the isoelectric point (IEP) of hematite, which was beneficial to the adsorption of the positively charged Pb(II) ion due to electrostatic attraction, and disadvantageous for adsorption of the negatively charged As(V). EXAFS analysis and DFT calculations confirmed that the local charge distribution was affected by the Fe vacancy defects, thereby influencing the adsorption affinities of hematite towards Pb(II) and As(V). In addition, PDOS and -COHP analysis further demonstrated that Fe vacancies in hematite considerably increased the bonding strength of As(V), while decreasing the bonding strength of Pb(II). The findings of this work not only aid in the rational design of highly efficient iron oxide adsorbents for heavy metal(loid) removal, but also assists in improving our abilities in predicting the migration riks of heavy metal(loid)s in complex soil and groundwater environments.

CRediT authorship contribution statement

Yongjin Xiang: Writing - original draft, Visualization, Methodology, Investigation, Formal analysis, Data curation, Conceptualization. **Juan Liu:** Resources, Data curation. **Yiwen Chen:** Software, Formal analysis, Data curation. **Hongjun Zhang:** Supervision, Methodology. **Lu Ren:** Resources, Investigation, Data curation. **Bangjiao Ye:** Supervision, Methodology. **Wenfeng Tan:** Writing - review & editing, Supervision. **Kappler Andreas:** Writing - review & editing, Supervision. **Jingtao Hou:** Writing - review & editing, Writing - original draft, Supervision, Project administration, Funding acquisition, Conceptualization.

Declaration of competing interest

The authors declare that they have no known competing financial interests or personal relationships that could have appeared to influence the work reported in this paper.

Data availability

The data that has been used is confidential.

Acknowledgments

This work was supported by the National Natural Science Foundation of China (41977022), Knowledge Innovation Program of Wuhan-Shuguang Project (2022020801020231), Natural Science Foundation of Hubei Province, China (2023AFD227), and the Fundamental Research Funds for the Central Universities (2662022YJ017). We thank Prof. Yuanzhi Li at Wuhan University of Technology for his help with DFT calculations and Beijing Synchrotron Radiation Facility (BSRF), China for EXAFS measurements at Beamline 1W1B. We also thank Prof. Marcelo Avena at Universidad Nacional del Sur (UNS)-CONICET for revising the original manuscript and providing some useful suggestions to improve the quality of this work.

Appendix A. Supplementary data

Supplementary data to this article can be found online at https://doi.org/10.1016/j.envpol.2024.123318.

References

Bargar, J.R., Brown, G.E., Parks, G.A., 1997. Surface complexation of Pb(II) at oxide-water interfaces: II. XAFS and bond-valence determination of mononuclear Pb(II) sorption products and surface functional groups on iron oxides. Geochem. Cosmochim. Acta 61, 2639–2652.

Bargar, J.R., Trainor, T.P., Fitts, J.P., Chambers, S.A., Brown, G.E., 2004. In situ grazing-incidence extended X-ray absorption fine structure study of Pb(II) chemisorption on hematite (0001) and (1-102) surfaces. Langmuir 20, 1667–1673.

Bocquet, S., Hill, A.J., 1995. Correlation of Néel temperature and vacancy defects in fine-particle goethites. Phys. Chem. Miner. 22, 524–528.

Burstein, G.T., 1992. Iron oxides in the laboratory, preparation and characterization. Corrosion Sci. 33.

Bylaska, E.J., Catalano, J.G., Mergelsberg, S.T., Saslow, S.A., Qafoku, O., Prange, M.P., Ilton, E.S., 2019. Association of defects and Zinc in hematite. Environ. Sci. Technol. 53, 13687–13694.

Chakrabarti, M., Banerjee, A., Sanyal, D., Sutradhar, M., Chakrabarti, A., 2008. Particle size dependence of optical and defect parameters in mechanically milled Fe_2O_3. J. Mater. Sci. 43, 4175–4181.

Chi, Z.L., Yu, G.H., Teng, H.H., Liu, H.G., Wang, J., Liu, C.Q., Shen, Q.R., Gadd, G.M., 2022. Molecular Trade-Offs between lattice oxygen and oxygen vacancy drive organic pollutant degradation in fungal Biomineralized Exoskeletons. Environ. Sci. Technol. 56, 8132–8141.

Ciotonea, C., Averlant, R.Ø., Rochard, G., Mamede, A., 2017. A simple and green procedure to prepare efficient manganese oxide nanopowder for the low temperature removal of formaldehyde. ChemCatChem 9, 2366–2376.

Cornell, R.M., Schwertmann, U., 2003. The Iron Oxides: Structure, Properties,reactions, Occurences and Uses. WILEY-VCH Verlag GmbH & Co. KGaA, Weinheim.

Du, H., Huang, Q., Lei, M., Tie, B., 2018. Sorption of Pb(II) by nanosized ferrihydrite organo-mineral composites formed by adsorption versus coprecipitation. ACS Earth Space Chem. 2, 556–564.

Du, H., Qu, C., Ma, M., Lei, M., Tie, B., Liu, X., Wei, X., Yang, Y., 2019. Insights into Pb(II) binding by Fe/Al hydroxide–microbe composite: XAFS spectroscopy and isothermal titration calorimetry study. Chem. Geol. 510, 84–90.

Dutta, S., Chattopadhyay, S., Jana, D., Banerjee, A., Manik, S., Pradhan, S.K., Sutradhar, M., Sarkar, A., 2006. Annealing effect on nano-ZnO powder studied from positron lifetime and optical absorption spectroscopy. J. Appl. Phys. 100, 114328.

Fang, L., Hong, Z., Borch, T., Shi, Q., Li, F., 2023. Iron vacancy accelerates Fe(II)-Induced anoxic as(III) oxidation coupled to iron reduction. Environ. Sci. Technol. 57, 2175–2185.

Guo, H., Stu, D., Berner, Z., 2007. Removal of arsenic from aqueous solution by natural siderite and hematite. Appl. Geochem. 22, 1039–1051.

Harsha, K., Senthil, P., Panda, R.C., 2019. A review on heavy metal pollution, toxicity and remedial measures: current trends and future perspectives. J. Mol. Liq. 290, 111197.

Hou, J., Luo, J., Hu, Z., Li, Y., Mao, M., Song, S., Liao, Q., Li, Q., 2016. Tremendous effect of oxygen vacancy defects on the oxidation of arsenite to arsenate on cryptomelane-type manganese oxide. Chem. Eng. J. 306, 597–606.

Hou, J., Tan, X., Xiang, Y., Zheng, Q., Chen, C., Sha, Z., Ren, L., Wang, M., Tan, W., 2022. Insights into the underlying effect of Fe vacancy defects on the adsorption affinity of goethite for arsenic immobilization. Environ. Pollut. 314, 120268.

Hou, J., Xiang, Y., Zheng, D., Li, Y., Xue, S., Wu, C., Hartley, W., Tan, W., 2017. Morphology-dependent enhancement of arsenite oxidation to arsenate on birnessite-type manganese oxide. Chem. Eng. J. 327, 235–243.

Ilton, E.S., Kovarik, L., Nakouzi, E., Mergelsberg, S.T., Mcbriarty, M.E., Bylaska, E.J., 2020. Using atom dynamics to map the defect structure around an impurity in nano-hematite. J. Phys. Chem. Lett. 11, 10396–10400.

Iorio, D.E., Cho, G.H., Liu, Y., Cheng, Z., Angelico, R., Colombo, C., 2018. Arsenate retention mechanisms on hematite with different morphologies evaluated using AFM, TEM measurements and vibrational spectroscopy. Geochem. Cosmochim. Acta 237, 155–170.

Jönsson, J., Sherman, D.M., 2008. Sorption of As(III) and As(V) to siderite, green rust (fougerite) and magnetite: implications for arsenic release in anoxic groundwaters. Chem. Geol. 255, 173–181.
Kong, M., Li, Y., Chen, X., Tian, T., Fang, P., Zheng, F., Zhao, X., 2011. Tuning the relative concentration ratio of bulk defects to surface defects in TiO_2 nanocrystals leads to high photocatalytic efficiency. J. Am. Chem. Soc. 133, 16414–16417.
Li, W., Liang, X., An, P., Feng, X., Tan, W., Qiu, G., 2016. Mechanisms on the morphology variation of hematite crystals by Al substitution: the modification of Fe and O reticular densities. Sci. Rep. 6, 1–10.
Li, Z., Ma, Z., Jan, T., Kuijp, V. Der, Yuan, Z., Huang, L., 2014. A review of soil heavy metal pollution from mines in China: pollution and health risk assessment. Sci. Total Environ. 468, 843–853.
Liang, Y., Xu, J., Koopal, L.K., Wang, M., Xiong, J., Hou, J., Tan, W., 2021. Facet-dependent surface charge and Pb^{2+} adsorption characteristics of hematite nanoparticles: CD-MUSIC-eSGC modeling. Environ. Res. 196, 110383.
Liu, C.H., Chuang, Y.H., Chen, T.Y., Tian, Y., Li, H., Wang, M.K., Zhang, W., 2015. Mechanism of arsenic adsorption on magnetite nanoparticles from water: thermodynamic and spectroscopic studies. Environ. Sci. Technol. 49, 7726–7734.
Liu, H., Lu, X., Li, M., Zhang, L., Pan, C., Zhang, R., Li, J., Xiang, W., 2018. Structural incorporation of manganese into goethite and its enhancement of Pb(II) adsorption. Environ. Sci. Technol. 52, 4719–4727.
Liu, X., Zhou, K., Wang, L., Wang, B., Li, Y., 2009. Oxygen vacancy clusters promoting reducibility and activity of ceria nanorods. J. Am. Chem. Soc. 131, 3140–3141.
Madsen, D.E., Cervera-Gontard, L., Kasama, T., Dunin-Borkowski, R.E., Koch, C.B., Hansen, M.F., Frandsen, C., Mørup, S., 2009. Magnetic fluctuations in nanosized goethite (α-FeOOH) grains. J. Phys. Condens. Matter 21, 016007.
Manas, D.S.Æ., Alok, S.Æ., 2008. Particle size dependence of optical and defect parameters in mechanically milled Fe2O3. J. Mater. Sci. 43, 4175–4181.
Mikutta, C., Kretzschmar, R., 2011. Spectroscopic evidence for ternary complex formation between arsenate and ferric iron complexes of humic substances. Environ. Sci. Technol. 45, 9550–9557.
Noerpel, M.R., Lee, S.S., Lenhart, J.J., 2016. X-ray analyses of lead adsorption on the (001), (110), and (012) hematite surfaces. Environ. Sci. Technol. 50, 12283–12291.
Notini, L., Byrne, J.M., Tomaszewski, E.J., Latta, D.E., Zhou, Z., Scherer, M.M., Kappler, A., 2019. Mineral defects enhance bioavailability of goethite toward microbial Fe(III) Reduction. Environ. Sci. Technol. 53, 8883–8891.
Notini, L., Latta, D.E., Neumann, A., Pearce, C.I., Sassi, M., N'Diaye, A.T., Rosso, K.M., Scherer, M.M., 2018. The role of defects in Fe(II)-Goethite electron transfer. Environ. Sci. Technol. 52, 2751–2759.
Qiu, C., Chen, W., Schmidt, M., Majs, F., Douglas, T.A., Trainor, T.P., 2020. Selective adsorption of Pb(II) on an Annealed hematite (1 1 02) surface: evidence from crystal truncation rod X-ray diffraction and density functional theory. Environ. Sci. Technol. 54, 6651–6660.
Roberts, H.E., Morris, K., Law, G.T.W., Mosselmans, J.F.W., Bots, P., Kvashnina, K., Shaw, S., 2017. Uranium(V) incorporation mechanisms and stability in Fe(II)/Fe(III) (oxyhydr)Oxides. Environ. Sci. Technol. Lett. 4, 421–426.
Santos, V.P., Pereira, M.F.R., Órfão, J.J.M., Figueiredo, J.L., 2010. The role of lattice oxygen on the activity of manganese oxides towards the oxidation of volatile organic compounds. Appl. Catal., B 99, 353–363.
Schwertmann, U., Cambier, P., Murad, E., 1985. Properties of goethites of varying crystallinity. Clay Clay Miner. 33, 369–378.
Tang, X., Chen, J., Chen, Y., 2023. A density functional based tight binding (DFTB+) study on the sulfidization-xanthate flotation mechanism of cerussite. Appl. Surf. Sci. 612, 155677.
Toner, B.M., Santelli, C.M., Marcus, M.A., Wirth, R., Chan, C.S., Mccollom, T., Bach, W., Edwards, K.J., 2009. Biogenic iron oxyhydroxide formation at mid-ocean ridge hydrothermal vents: Juan de Fuca Ridge. Geochem. Cosmochim. Acta 73, 388–403.
Van Genuchten, C.M., Addy, S.E.A., Peña, J., Gadgil, A.J., 2012. Removing arsenic from synthetic groundwater with iron electrocoagulation: an Fe and as K-edge EXAFS study. Environ. Sci. Technol. 46, 986–994.
Wang, Y., Morin, G., Ona-Nguema, G., Juillot, F., Calas, G., Brown, G.E., 2011. Distinctive arsenic(V) trapping modes by magnetite nanoparticles induced by different sorption processes. Environ. Sci. Technol. 45, 7258–7266.
Xue, Q., Ran, Y., Tan, Y., Peacock, C.L., Du, H., 2019. Arsenite and arsenate binding to ferrihydrite organo-mineral coprecipitate: Implications for arsenic mobility and fate in natural environments. Chemosphere 224, 103–110.
Yan, L., Chan, T., Jing, C., 2021. Mechanistic study for Antimony adsorption and precipitation on hematite facets. Environ. Sci. Technol. 56, 3138–3146.
Yan, L., Chan, T., Jing, C., 2020. Arsenic adsorption on hematite facets: spectroscopy and DFT study. Environ. Sci.: Nano 7, 3927–3939.
Zhang, B.Q., Lu, L., Lai, M.O., 2003. Evolution of vacancy densities in powder particles during mechanical milling. Phys. B Condens. Matter 325, 120–129.
Zheng, Q., Tu, S., Chen, Y., Zhang, H., Hartley, W., Ye, B., Ren, L., Xiong, J., Tan, W., Kappler, A., Hou, J., 2023. Micropore sites in ferrihydrite are responsible for its higher affinity towards As(III) relative to As(V). Geochem. Cosmochim. Acta 348, 27–40.